

In situ Investigation of Oxide Films on Zirconium Alloy in PWR Primary Water Chemistry

Taeho Kim^a, Kyoung Joon Choi^a, Seung Chang Yoo^a, and Ji Hyun Kim^{a*}

^a School of Mechanical and Nuclear Engineering Ulsan National Institute of Science and Technology (UNIST),
Ulju-gun, Ulsan 689-798, Republic of Korea

*Corresponding author: kimjh@unist.ac.kr

1. Introduction

Zirconium alloys are used as fuel cladding materials in nuclear power reactors, because these materials have a very low thermal neutron capture cross section as well as desirable mechanical properties. However, the Fukushima accident shows that the oxidation behavior of zirconium alloy is an important issue because the zirconium alloy functions as a shield of nuclear material (i.e., uranium, fission gas), and the degradation on zirconium cladding directly causes severe accident on nuclear power plant. Therefore, to ensure the safety of nuclear power reactors, the performance and sustainability of nuclear fuel should be understood.

Currently, the water-metal interface is regarded as the rate-controlling site governing the rapid oxidation transition in high-burn-up fuels [1-4]. Zirconium oxide is formed at the water-metal interface, and its structure and phase play an important role in determining its mechanical properties [5-18]. During the oxidation process, a protective tetragonal oxide layer develops at the interface owing to the accumulated high stress. This layer turns into a non-protective one of monoclinic zirconium oxide as the layer thickness increases, thus decreasing the stress [16-18]. Therefore, it is important to determine the types of oxides (i.e., the phases of the oxides) in the oxide layer formed on the zirconium alloy during the in situ oxidation process. Because it does not require the removal of specimen from the oxidation environment, which can modify the oxide phase and structure on specimen.

Raman spectroscopy can be applied the in situ investigation, because the experimental system can be conducted at elevated temperatures and high pressure. In situ Raman spectroscopy identify the oxide phase and oxidation products on a metal surface w for comprehensive understanding of the oxidation mechanism. It involves measuring the wavelength and intensity of inelastically scattered light due to the excitation of molecules when the test sample is irradiated with a laser. The light inelastically scattered by the sample is collected. The shift in its energy from that of the incident light, which is by a discrete amount, is characteristic of the scattering material [19, 20]. There have been a number of studies involving the ex situ Raman analyses of zirconium and zirconium alloys in aqueous solutions [21-25]. Also, in previous studies [19, 20, 26], the in situ Raman system was designed for the oxide analysis on nickel base alloy and low alloy

steel in high temperature environment. Also, the dissolved hydrogen (DH) concentration effect on the oxide has been investigated by other previous research [27-29]. However, the in situ Raman investigation of zirconium oxide and alloy at high temperature water environment with various DH concentration was conducted relatively little number compared with other metal alloy.

Therefore, in this study, the zirconium alloy was oxidized in situ at different DH concentrations, including under the normal operating conditions of a pressurized water reactor (PWR) (30 cc/kg) and at a higher DH concentration (50 cc/kg) at high temperature water. Next, in situ Raman spectroscopy was used to characterize oxide phase at the zirconium-water interface, and the effects of the DH concentration on the characteristics of the phase of the zirconium oxide were investigated. Then, the ex situ investigation methods like scanning electron microscopy (SEM), energy dispersive X-ray spectroscopy (EDS) and transmission electron microscopy (TEM) were used for characterizing the oxide structure of zirconium alloy.

2. EXPERIMENTAL

2.1 Materials and specimen preparation

A plate of the zirconium alloy, ZIRLO [30-32] provided by KEPSCO Nuclear Fuel Co., Ltd., was used in this study, for oxidation in the primary water environment of a PWR. The chemical composition of ZIRLO is explained in the Table 1, and the dimension of specimen was 40 mm × 40 mm × 0.65 mm, and the specimen was polished before the oxidization process.

First, SiC papers with grits 400 to 800 were used to polish the specimen. Next, it was polished using diamond pastes (up to 1 μm). Finally, to minimize the mechanical transformation of the ZIRLO specimen, a 0.05 μm colloidal silica paste was used for polishing.

2.2 Experimental system

To simulate the primary water chemistry of a PWR, a loop for the high-temperature and high-pressure conditions and an autoclave were used. A schematic of the complete system used for the in situ Raman spectroscopic analysis is shown in Fig. 1(a), and the region near the specimen in the autoclave is shown in Fig. 1(b). Using this system, the primary

Table 1. Chemical composition of ZIRLO

Element	Nb	Sn	Fe	Hf	C	O	N	Zr
Composition (wt %)	0.96	0.76	0.18	0.002	0.1	0.62	0.03	Balance

water chemistry of the simulated PWR was set as follows: temperature of 325 °C, pressure of 18 MPa, by main and pre heaters and high pressure pump, dissolved oxygen concentration of less than 5 ppb, and LiOH and H₃BO₃ concentrations of 2 and 1200 ppm, respectively, and it is maintained during oxidation process. The water chemistry data during oxidation including electrical conductivity of inlet and outlet water, dissolved oxygen and hydrogen concentration, autoclave pressure and temperature are shown in Fig. 2. Also, the DH concentration was precisely measured by Orbisphere™ DH sensor.

2.3 In situ Raman spectroscopic system

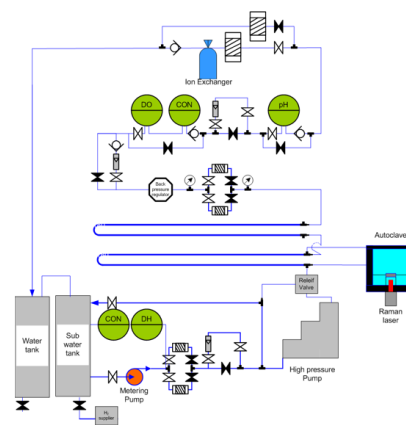
The Raman spectroscopy measurements were made using a RamanRXNTM, manufactured by Kaiser optical systems Inc., which uses a 532 nm wavelength krypton ion laser with a maximum power 100 mW. The irradiation area in the specimen of the Raman system was 100 μm² and the power density at the specimen was less than 10 mW/cm² to prevent the damage on specimen. The in situ Raman system consists of four parts, and these include the immersion optics for moving the laser toward the sample, a notch filter for signal processing, a band-pass filter, and a charge-coupled device detector, and the detail explanation about Raman system is shown in earlier studies [19, 20]. The optical probe for in situ Raman was installed in the autoclave within the distance under 1 mm, which is lower than the maximum focal length of laser beam.

2.4 Experimental procedure

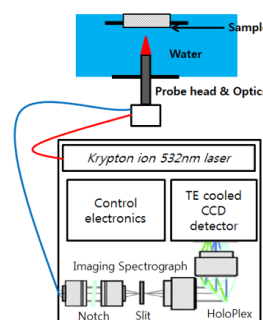
In this study, in situ Raman spectroscopic measurement was performed on ZIRLO specimen in primary water environment. The temperature was measured by thermocouples positioned close to the specimen in the autoclave, and the ZIRLO plate specimen was oxidized under primary water chemistry conditions for 150 h. Tests were conducted in an autoclave system specially constructed for the present study. Careful consideration was given to ensuring extremely rigorous chemistry control, and near-theoretical water conductivity was achieved routinely.

DH concentration was maintained at 50 cc/kg during 120 h oxidation, then the DH concentration was decreased to 30 cc/kg, and the detail explanation is shown in Fig. 2. At DH concentration is 50 cc/kg, the in situ Raman spectra were obtained after 60 h and after 120 h, respectively. Also the in situ Raman spectrum measurement was made at DH concentration is 30 cc/kg to see the effect of DH concentration change

on oxidation behavior of ZIRLO in high temperature water, and the in situ Raman spectrum was obtained after 140 h from oxidation start-up. During each measurement, the in situ Raman spectra were recorded over a period of 30 minutes and it was repeated 2 times for increasing the signal-to-noise ratio. Before analyzing the in situ Raman spectra, the post treatments like smoothing process using Svizy-Golay method and baseline correction method were conducted. After in situ Raman spectra measurement, the ZIRLO specimen was cooled down to room temperature in the autoclave and removed for additional ex situ investigation. As the ex situ investigation, it was performed to characterize the oxide layer of specimen using the several instruments like SEM, EDS and TEM. For TEM analysis, focused ion beam (FIB) method is used for making analysis sample. To prevent the surface contamination from impurities and ion beam damage during the FIB process, the specimen surface was coated with sputtered carbon before the FIB process. And, the in situ and ex situ results were compared for a comprehensive understanding of the zirconium oxide characteristic.



(a) Schematic of the complete system used for the Raman spectroscopic analysis



(b) Region near the ZIRLO sample in autoclave

Figure 1. Schematic figure of the system used for zirconium alloy oxidation test.

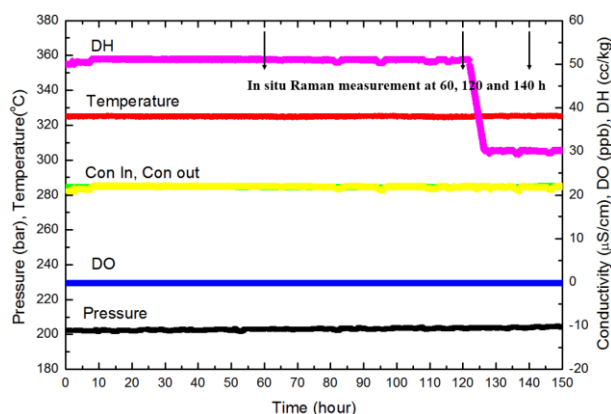


Figure 2. Water chemistry data and in-situ Raman measurement time during oxidation.

3. RESULTS AND DISCUSSION

3.1. Reference Raman spectra for zirconium oxide powders in room temperature air

The ex situ Raman spectra of reference powder sample, produced in Sigma-Aldrich, is measured in room temperature air environment with 532 nm radiation. Figure 3 shows the Raman spectrum for ZrO_2 powder (99.9%). The measured Raman spectrum for ZrO_2 powder in this study exhibited features at 334, 347, 382, 475, 558, 633 and 756 cm^{-1} , and these are summarized in Table 2 in comparison with earlier studies [11, 33, 34]. Features below 300 cm^{-1} are not shown because the Raman spectrum exhibits a relatively high background noise due to oxygen and nitrogen Raman lines. These results were well matched with monoclinic zirconium oxide phase in literature [11, 33, 34]. It is considered that the slight difference between the current work and Maslar et al.'s work [11] is caused by the difference of laser wavelength. Maslar et al. [11] used 514.5 nm argon ion laser, but in this study, 532 nm laser is used.

3.2. In situ Raman spectroscopy at high temperature water

Figure 4 shows the in situ Raman spectra of the zirconium alloy specimen oxidized for 120 h while the DH concentration was maintained at 50 cc/kg. The baseline correction method was applied to remove the baseline drift caused by fluorescence. From this method, it is possible to obtain the better Raman spectrum. The strong intensity peaks, originated from sapphire window and boric acid, are marked in the spectrum. The results of Raman spectra in high temperature water environment at DH 50 cc/kg and 30 cc/kg are also summarized in Table 3 and 4. The sapphire window, which is attached to the tip, produced Raman peaks at 414 and 747 cm^{-1} . Also, the peaks related to the boric acid which is dissolved in water, are observed in the range of 868–870 cm^{-1} [19, 20, 26]. The lower

line in red is the Raman spectrum of the zirconium alloy specimen oxidized for 60 h. The arrows mark the peaks related to zirconium oxide, especially monoclinic and tetragonal phase. The peaks at 329, 380, 558 and 637 cm^{-1} can be attributed to monoclinic zirconium oxide phase, and the peak at 470 cm^{-1} can be attributed to tetragonal zirconium oxide phase. In this data, the signal-to-noise ratio was so small that it made difficult to analyze the peaks accurately. It is due to that the oxidation time is not long enough to make oxide layer on zirconium alloy specimen.

The upper line in black is the Raman spectrum obtained after 120 h, the signal-to-noise ratio was larger because of the rearrangement of immersion optics in the autoclave and the oxidation time increase. Thus, it was possible to identify the shift in the Raman peaks. The peaks of tetragonal zirconium oxide decreased in intensity as the zirconium oxide layer increased in thickness during oxidation process. As comparing two in situ Raman spectra, the oxidation time is considered as one of key variables to determine the phase of the oxide. In the early stage of the oxidation process, the zirconium oxide layer exhibits both monoclinic and tetragonal phases. The peaks of monoclinic zirconium oxide, 329, 380, 558, and 637 cm^{-1} are shown and the peak of tetragonal zirconium oxide, 470 cm^{-1} is shown. The possible phase of zirconium oxide formed under the primary water chemistry conditions at 325 °C is illustrated in oxygen-zirconium phase diagram, in Fig. 5 [35]. As can be seen from the Fig. 5, the monoclinic phase of ZrO_2 is the most stable one at 600 K (327 °C). While monoclinic ZrO_2 was found in this study, a simulation of the oxidation process also suggested that monoclinic ZrO_2 is formed on the surface of the ZIRLO specimen [17], and the in situ Raman spectra show that the monoclinic phase is the dominant zirconium oxide at the early stage oxidation.

Next, it is determined the Raman spectra of ZIRLO specimens corresponding to different DH concentrations. The DH concentration was changed from 50 cc/kg to 30 cc/kg, and the in situ Raman spectrum was obtained after the DH concentration was stabilized. As can be seen from Fig. 6, Raman peaks for the sapphire window were observed at 414 and 747 cm^{-1} , also the peak at 868 – 870 cm^{-1} is attributed to the boric acid. The upper line is the Raman spectrum corresponding to a DH of 30 cc/kg while the lower line is the spectrum corresponding to a DH of 50 cc/kg. The in situ Raman spectrum measured at 30 cc/kg shows different spectrum to 50 cc/kg result. In 30 cc/kg result, a new and broad range monoclinic zirconium oxide peaks are shown in 530 – 561 cm^{-1} , and the tetragonal zirconium oxide peak at 470 cm^{-1} is slightly stronger than 50 cc/kg Raman spectrum. Also peaks at 380 and 756 cm^{-1} in 30 cc/kg Raman spectrum which can be attributed to monoclinic zirconium oxide are much stronger than 50 cc/kg Raman spectrum, and it shows

that the zirconium oxide does undergo a phase change when the DH is changed.

Results from Raman spectroscopy of different DH concentration environment, 30 cc/kg and 50 cc/kg show that the monoclinic phase zirconium oxide is much dominant when the DH is 30 cc/kg. As shown in Fig. 6, the 380 and 637 cm^{-1} peaks are larger and the new broad peak between 530 and 561 cm^{-1} appears. This is an evidence of the monoclinic phase is stable at 30 cc/kg DH concentration environment. Also the minor peak of monoclinic zirconium oxide like 333 cm^{-1} and the peak which is overlapped with sapphire at 756 cm^{-1} exist. In order to verify the information of zirconium oxide phases obtained by in-situ Raman spectroscopy with oxidized ZIRLO specimen, SEM and TEM analysis were conducted and the comparison with their results will provide in the latter section.

Table 2. Results of ex situ Raman peaks of ZrO_2 powder in room temperature air environment (cm^{-1})

ZrO_2 powder	Zirconium oxide phase	Ref. [11]	Ref. [33]	Ref. [34]
334	Monoclinic	333	334	335
347	Monoclinic	347	349	348
382	Monoclinic	382	380	385
475	Monoclinic	475	476	480
558	Monoclinic	558	558	558
633	Monoclinic	637	638	Not shown
756	Monoclinic	756	757	Not shown

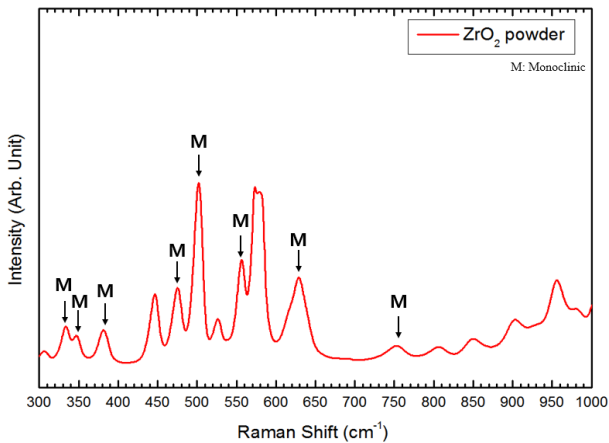


Figure 3. Measured Raman spectrum of reference zirconium oxide powders excited by a laser at 532 nm in air.

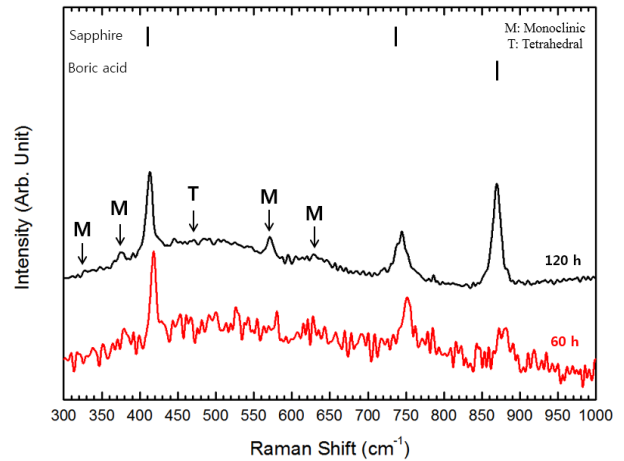


Figure 4. In-situ Raman spectra of oxidized ZIRLO specimen for different oxidation times (DH = 50 cc/kg; upper line = 120 h; lower line = 60 h).

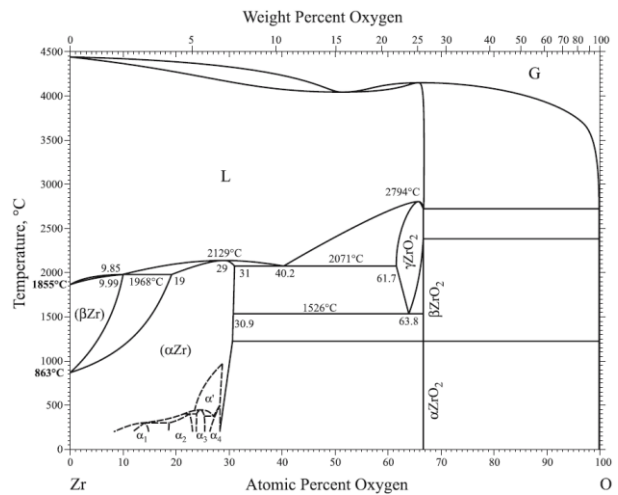


Figure 5. Oxygen-zirconium phase diagram [35].

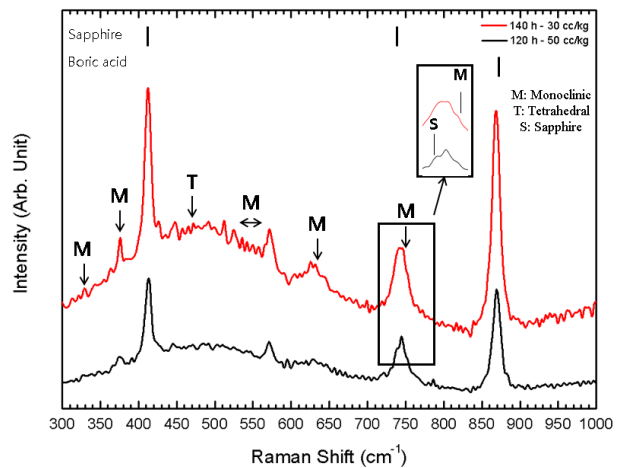


Figure 6. In situ Raman spectra of oxidized ZIRLO specimen corresponding to two different DH concentrations (upper line: DH = 30 cc/kg; lower line: DH = 50 cc/kg).

Table 3. Results of in situ Raman peaks of oxidized ZIRLO (cm^{-1}) (DH=50 cc/kg)

Oxidized ZIRLO	Zirconium oxide		Ref. [11]	Ref. [33]
	phase			
329	Monoclinic		333	334
380	Monoclinic		382	380
470	Tetragonal		-	473
558	Monoclinic		558	558
637	Monoclinic		637	638

Table 4. Results of in situ Raman peaks of oxidized ZIRLO (cm^{-1}) (DH=30 cc/kg)

Oxidized ZIRLO	Zirconium oxide		Ref. [11]	Ref. [33]
	phase			
329	Monoclinic		333	334
380	Monoclinic		382	380
470	Tetragonal		-	473
530 – 561 (Broad range)	Monoclinic		558	558
637	Monoclinic		637	638
756	Monoclinic		756	757

3.3. Ex situ characterization of zirconium oxide

Ex situ characterization of oxide on zirconium alloy specimen removed from the autoclave were performed using Ex-situ Raman, SEM and EDS to validate in situ Raman results. Figure 7 shows the measured ex situ Raman spectrum of oxidized ZIRLO specimen at room temperature in air environment, and the results of Raman spectrum is summarized in Table 5. The Raman peaks for oxidized ZIRLO specimen are observed at 335, 384, 477, 502, 538, 554, 636 and 751 cm^{-1} and these peaks can be attributed to monoclinic zirconium oxide. Feature at and 335 cm^{-1} are assigned to vibrations which do not involve oxygen atoms, and it means they are zirconium-zirconium atom vibration modes [33]. Then, the four peaks at 384, 477, 502 and 638 cm^{-1} are assigned to oxygen-oxygen atom vibration mode [33]. The Raman spectrum of ZIRLO specimen is slightly different when it is measured at in situ environment and air environment. The signal to noise ratio is significantly improved because of the absence of boric acid peak and environmental noise. The ca. 751 cm^{-1} peak in the ex situ spectrum was weakened by the absence of sapphire window which is installed in immersion optics for in situ measurement. Also, it is

difficult to find the peaks of tetragonal phase oxide, because the monoclinic phase is the most stable phase at the room temperature, discussed in Okamoto et al.'s work [35] and the tetragonal zirconium oxide Raman peaks are similar to monoclinic zirconium's peak [11, 33, 36].

The difference in peaks between in situ and ex situ Raman measurement originated from the environment difference. The Raman peaks at 384, 538, 554 and 638 cm^{-1} are both shown and they can be attributed to monoclinic zirconium oxide. However, there is a slight difference between the two Raman spectra, especially, at 335, 470 and 477 cm^{-1} . The peak at 477 cm^{-1} which is attributed to tetragonal zirconium oxide phase is shown in situ Raman spectrum after 140 h oxidation, whereas it does not appear at ex situ Raman spectrum. The extinction of tetragonal phase and increase of monoclinic phase related peaks are due to the cooling of specimen to room temperature. Also, the monoclinic zirconium oxide peaks at 335 and 470 cm^{-1} become much stronger at ex situ Raman spectrum. Furthermore, the peaks which are associated with sapphire window and boric acid are not observed because the sapphire window for immersion optics is not required for ex situ Raman spectroscopy. Therefore, the peak at ca. 750 which can be attributed monoclinic zirconium oxide is easily distinguished compared to in situ Raman spectrum. Note that the measurement temperature and environment have a decisive effect on zirconium oxide, especially its phase, and the Raman spectrum result.

Figure 8 represents the SEM image and EDS profile of cross section of the oxidized ZIRLO specimen. The SEM analysis in Fig. 8(a) indicates that the zirconium oxide was formed on the zirconium alloy and its thickness after 150 h oxidation is approximately 1.2 μm or less. The EDS analysis was conducted and the result is shown in Fig. 8(b). Figure 8(b) indicates that the composition of zirconium oxide is 65 ~ 69 atomic % oxygen and 31 ~ 35 atomic % zirconium. And, the thickness of oxide layer is 1.2 μm .

The oxidized ZIRLO specimen was investigated by using TEM analysis after the specimen is prepared by using the FIB method. Figure 9(a) represents the result of TEM micrograph, as shown in Fig. 9(a), and it is found that there exist the crack (white line) on the oxide/metal interface. The arrowed mark on Fig. 9(a) means the oxide growth direction. The size of crack is around 200 nm and the cracks are parallel to the oxide/metal interface, and they have undulating shape. The hand-drawn sketch of the grain boundary is shown in Fig. 9(b). In the oxide formed on zirconium alloy, both equiaxed and columnar shape grains were observed. The diameter of the equiaxed grains is 15 – 25 nm and the width of the columnar grains is 20 – 40 nm. The columnar shape grains are positioned near the oxide/metal interface, however, the equiaxed shape grains are positioned at the end of zirconium oxide layer. Figure 10 shows the TEM-EDS analysis result of

oxidized zirconium alloy. The undulating oxide/metal interface is shown in Fig. 10 and the zirconium oxide was formed on the interface. The results of maps of the chemical composition of cross section of specimen shows the distinct interface line between oxide and metal.

Diffraction pattern analysis using fast Fourier transform (FFT) method is conducted to confirm the zirconium oxide phases which are different depending on the grain shape. The diffraction patterns are obtained at two different position A and B in Fig. 9(a), and A represents the equiaxed shape grain, and B represents the columnar shape grain. The two high resolution TEM (HRTEM) images of at position A and B are represented in Fig. 11. Figure 11 clearly shows that there are disordered amorphous zirconium oxide layer, and to fully understand the oxide phase of them, the FFT images are obtained. Figure 11(a) is the FFT image of position A, and Fig. 11(b) is the FFT image of position B. The d-spacing of position A and B are explained in Table 6 and the phase of them are decided using JCPDS diffraction reference data (42-1164, 50-1087, 37-1484; Zirconium oxide).

The dominant zirconium oxide phases of position A are (110), (101) tetragonal phase, and the minor $(\bar{1}11)$ monoclinic phase is shown. The d-spacing of (110) tetragonal phase oxide is ca 0.257 nm, it of (101) tetragonal phase oxide is ca 0.300 nm and it of $(\bar{1}11)$ monoclinic phase oxide is ca 0.316 nm, therefore, it can be seen that there are good agreements between the results in this study and reference data. The dominant zirconium oxide phases of position B is $(\bar{2}01)$, (111), and $(\bar{2}10)$ monoclinic phase and they have same ratio of total diffraction pattern. The d-spacing of $(\bar{2}01)$ monoclinic phase oxide is ca 0.250 nm, it of (111) monoclinic phase oxide is ca 0.284 nm, and it of $(\bar{2}10)$ monoclinic phase oxide is ca 0.234 nm. Also it is well matched with the reference data. This results shows that the equiaxed shape grain is mainly tetragonal phase oxide and the columnar shape grain is mainly monoclinic phase oxide.

Ex situ investigation results using SEM, TEM represent the thickness of oxide after 150 h oxidation is around 1.2 μm , which is shown in Fig. 8, 9 and 10. In Fig. 9(a), the 200 nm size cracks are positioned on the oxide/metal interface, which are parallel to interface. Moreover, Fig. 9(a) shows that the two types of zirconium oxide grains are existed and they are composed with equiaxed and columnar shape grain, and to make it easy to identify, the hand-drawn sketch is represented in Fig. 9(b). In previous literature [7, 13, 14], the grain structure of zirconium oxide, which is formed at pressurized water reactor chemistry is consisted of equiaxed and columnar shape grain. The equiaxed shape grain is positioned at upper part of

zirconium oxide and the columnar shape grain is located near the oxide/metal interface. It can be seen in Fig. 9 that the results show good agreements between the TEM images in this study and literature data. Also, the sizes of columnar grains are measured, the average length of columnar shape is around 500 nm. As discussed in previous study [37], equiaxed shape grains were formed at the early stage of oxidation, and the columnar shape grains were grown in order to decrease the compressive stress of oxide structure, and it is well matched the oxide growth direction, red marked arrow in Fig. 9(a).

Figure 11(a) and (b) are the HRTEM images of zirconium oxide at specific position A and B, marked in Fig. 9 (a). The amorphous zirconium oxide is shown in Fig. 10, and to investigate the difference of oxide phase at different oxide grain structure, the further analysis is conducted. First, the position A and B are represented each zirconium oxide grain structure, position A represents equiaxed shape grain, and position B does columnar shape grain. For identifying the phase and the crystallinity of the zirconium oxide at specific position, the FFT imaging method is used in this study. Figure 11 shows the FFT image of zirconium oxide, and as discussed in above paragraph, the position A is mainly consisted of tetragonal phase zirconium oxide and the position B is monoclinic phase zirconium oxide. It is important that there are several planes of zirconium oxide, however, the phase of oxide is decided by the grain shape of zirconium oxide. Kim et al. [37] also mentioned that the equiaxed part zirconium oxide is mainly tetragonal phase and the columnar part is mainly monoclinic phase zirconium oxide, and it is due to the applied stress in the tetragonal phase. The relaxation of stress makes tetragonal phase transform to monoclinic phase oxide at the oxide/metal interface [38].

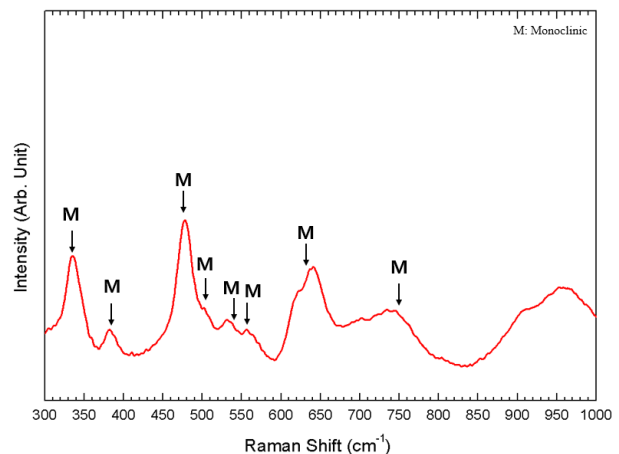


Figure 7. Ex situ Raman spectrum of the oxidized ZIRLO specimen at room temperature in air.

4. CONCLUSION

In this study, the in situ Raman spectroscopy is conducted for investigating the effects of the DH

concentration on the phase of the zirconium oxide layer formed at the water-zirconium interface under PWR conditions. In the early stage of the oxidation process, zirconium oxide with both tetragonal and monoclinic phases is formed. With an increase in the oxidation time to 150 h, the unstable tetragonal phase disappears and the monoclinic phase is dominant and possibly because of the stress relaxation according to previous and present results. From this study, the following conclusions are made:

Table 5. Results of ex situ Raman peaks of oxidized ZIRLO after 150 h oxidation (cm^{-1})

Oxidized ZIRLO	Zirconium oxide		Ref. [11]	Ref. [33]
	phase			
335	Monoclinic		333	334
384	Monoclinic		382	380
477	Monoclinic		475	476
502	Monoclinic		502	503
538	Monoclinic		538	539
554	Monoclinic		558	558
638	Monoclinic		637	638
751	Monoclinic		756	757

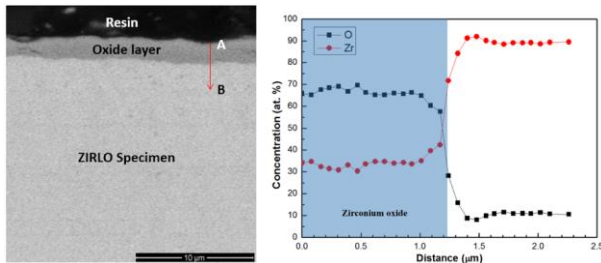
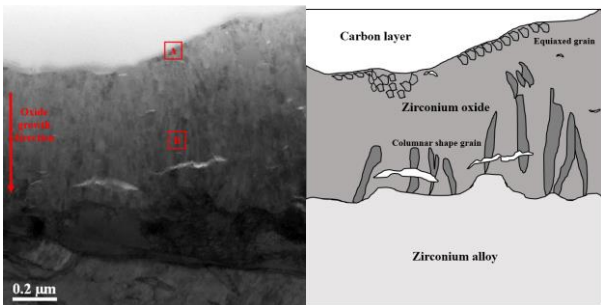


Figure 8. SEM image and EDS profile of the oxide film on ZIRLO specimen after 150 h oxidation.



(a) TEM image of oxide film on ZIRLO specimen after 150 h oxidation, (b) Hand-drawn sketch of oxide film on ZIRLO specimen after 150 h oxidation

Figure 9. TEM micrograph and sketch of oxide film on ZIRLO specimen.

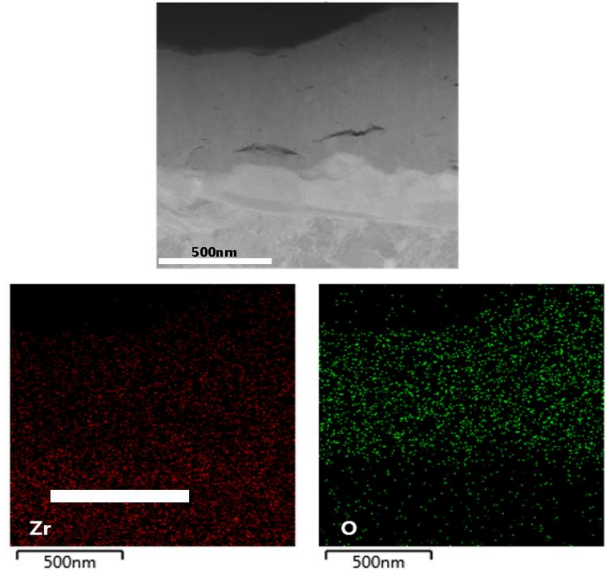
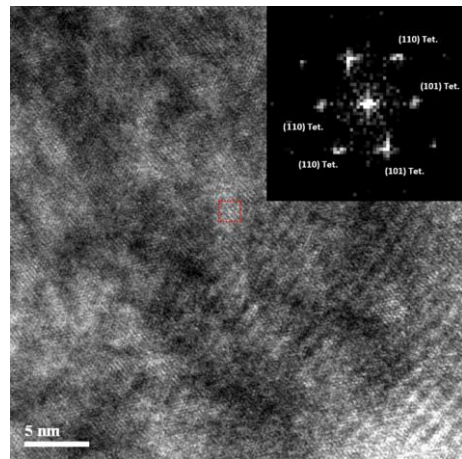
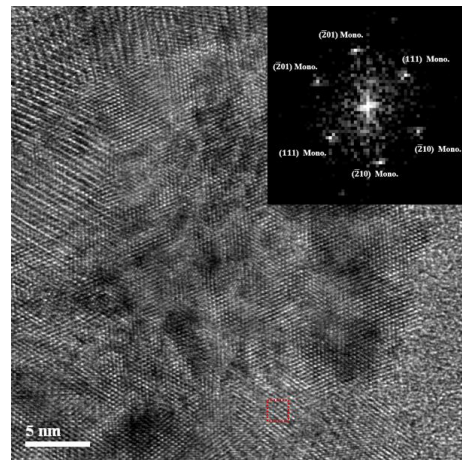


Figure 10. TEM image and maps of cross sectional composition in the oxide layer formed on ZIRLO specimen after 150 h oxidation



(a) HRTEM and FFT image of position A



(b) HRTEM and FFT image of position B

Figure 11. HRTEM and FFT images of oxidized ZIRLO specimen at specific position A and B indicated in Fig. 9.

Table 6. d-spacing of oxidized ZIRLO at two different positions (A and B) indicated in Fig. 9

d-spacing of A (nm)	Zirconium oxide phase	d-spacing of B (nm)	Zirconium oxide phase
0.3016	Unidentified	0.2481	($\bar{2}01$) Monoclinic
0.2567	(110) Tetragonal	0.2820	(111) Monoclinic
0.3047	(101) Tetragonal	0.2383	($\bar{2}10$) Monoclinic
0.2889	(101) Tetragonal	0.2350	($\bar{2}10$) Monoclinic
0.2556	(110) Tetragonal	0.2847	(111) Monoclinic
0.3117	($\bar{1}11$) Monoclinic	0.2490	($\bar{2}01$) Monoclinic

1. Results from in situ Raman spectroscopy under different DH concentration environment, 30 cc/kg and 50 cc/kg show that the monoclinic phase zirconium oxide is dominant when the DH is 30 cc/kg. Especially, a new and broad range monoclinic zirconium oxide peaks appear at 530 – 561 cm^{-1} in 30 cc/kg Raman spectrum. Also, peaks at 380 and 765 cm^{-1} can be attributed to monoclinic zirconium oxide phase are slightly stronger than 50 cc/kg Raman spectrum.

2. In ex situ Raman spectrum, the peaks attributed to tetragonal zirconium oxide phase disappear, and the peak intensity of monoclinic zirconium oxide phase is highly increased, due to the temperature and environment change of Raman measurement.

3. In SEM image, the oxide thickness is around 1.2 μm and the EDS image supports it. In TEM image, the more detail oxide structure of zirconium oxide is shown, the 200 nm size cracks are positioned above the oxide/metal interface.

4. FFT images show that the zirconium oxide is not a single crystal, amorphous oxide. The equiaxed grain is mainly consisted of tetragonal phase zirconium oxide and the columnar grain is monoclinic phase.

ACKNOWLEDGMENT

This work was financially supported by the International Collaborative Energy Technology R&D Program (No. 20138530030010), and by the Nuclear Power Core Technology Development Program (No.2012T100201562) of the Korea Institute of Energy Technology Evaluation and Planning (KETEP) which is funded by the Ministry of Trade Industry and Energy.

REFERENCES

[1] F. Garzarolli, H. Seidel, R. Tricot, J. Gros. Oxide growth mechanism on zirconium alloys, ASTM STP. 1132 (1991) 395.
[2] H. Beie, F. Garzarolli, H. Ruhmann, H. Sell, A. Mitwalsky. Examinations of the corrosion mechanism of zirconium alloys. Zirconium in the nuclear industry:

Tenth international symposium. ASTM STP. 1245 (1994) 818.

[3] H. Anada, K. Takeda. Microstructure of oxides on Zircaloy-4, 1.0 Nb Zircaloy-4, and Zircaloy-2 formed in 10.3-MPa steam at 673 K, ASTM STP. 1295 (1996) 35.

[4] S. Abolhassani, R. Restani, T. Rebac, F. Groeschel, W. Hoffelner, G. Bart, W. Goll, F. Aeschbach. TEM examinations of the metal-oxide interface of zirconium based alloys irradiated in a pressurized water reactor, ASTM STP. 1467 (2006) 467.

[5] J.E. Maslar, W.S. Hurst, W.J. Bowers Jr, J.H. Hendricks, In situ Raman spectroscopic investigation of zirconium–niobium alloy corrosion under hydrothermal conditions, J. Nucl. Mater. 298 (2001) 239.

[6] M. Oskarsson, E. Ahlberg, K. Pettersson, Oxidation of Zircaloy-2 and Zircaloy-4 in water and lithiated water at 360°C, J. Nucl. Mater. 295 (2001) 97.

[7] P. Bouvier, J. Godlewski, G. Lucazeau, A Raman study of the nanocrystallite size effect on the pressure–temperature phase diagram of zirconia grown by zirconium-based alloys oxidation, J. Nucl. Mater. 300 (2002) 118.

[8] A. Yilmazbayhan, A.T. Motta, R.J. Comstock, G.P. Sabol, B. Lai, Z. Cai, Structure of zirconium alloy oxides formed in pure water studied with synchrotron radiation and optical microscopy: relation to corrosion rate, J. Nucl. Mater. 324 (2004) 6.

[9] B. Cox, Some thoughts on the mechanisms of in-reactor corrosion of zirconium alloys, J. Nucl. Mater. 336 (2005) 331.

[10] A. Yilmazbayhan, E. Breval, A.T. Motta, R.J. Comstock, Transmission electron microscopy examination of oxide layers formed on Zr alloys, J. Nucl. Mater. 349 (2006) 265.

[11] H.X. Zhang, D. Fruchart, E.K. Hlil, L. Ortega, Z.K. Li, J.J. Zhang, J. Sun, L. Zhou, Crystal structure, corrosion kinetics of new zirconium alloys and residual stress analysis of oxide films, J. Nucl. Mater. 396 (2010) 65.

[12] J. Wei, P. Frankel, E. Polatidis, M. Blat, A. Ambard, R. Comstock, L. Hallstadius, D. Hudson, G. Smith, C. Grovenor, The effect of Sn on autoclave corrosion performance and corrosion mechanisms in Zr–Sn–Nb alloys, Acta Mater. 61 (2013) 4200.

[13] A. Couet, A.T. Motta, R.J. Comstock, Hydrogen pickup measurements in zirconium alloys: Relation to oxidation kinetics, J. Nucl. Mater. 451 (2014) 1.

[14] X. He, H. Yu, G. Jiang, G. Dang, D. Wu, Y. Zhang, Cladding oxidation model development based on diffusion equations and a simulation of the monoclinic-tetragonal phase transformation of zirconia during transient oxidation, J. Nucl. Mater. 451 (2014) 55.

[15] B. de Gabory, A.T. Motta, K. Wang, Transmission electron microscopy characterization of Zircaloy-4 and ZIRLO™ oxide layers, J. Nucl. Mater. 456 (2015) 272.

- [16] W. Qin, C. Nam, H.L. Li, J.A. Szipunar, Tetragonal phase stability in ZrO₂ film formed on zirconium alloys and its effects on corrosion resistance, *Acta Mater.* 55 (2007) 1695.
- [17] E. Polatidis, P. Frankel, J. Wei, M. Klaus, R.J. Comstock, A. Ambard, S. Lyon, R.A. Cottis, M. Preuss, Residual stresses and tetragonal phase fraction characterisation of corrosion tested Zircaloy-4 using energy dispersive synchrotron X-ray diffraction, *J. Nucl. Mater.* 432 (2013) 102.
- [18] P. Platt, E. Polatidis, P. Frankel, M. Klaus, M. Gass, R. Howells, M. Preuss, A study into stress relaxation in oxides formed on zirconium alloys, *J. Nucl. Mater.* 456 (2015) 415.
- [19] J. Kim, K.J. Choi, C.B. Bahn, J.H. Kim, In situ Raman spectroscopic analysis of surface oxide films on Ni-base alloy/low alloy steel dissimilar metal weld interfaces in high-temperature water, *J. Nucl. Mater.* 449 (2014) 181.
- [20] J. Kim, S.H. Kim, K.J. Choi, C.B. Bahn, I.S. Hwang, J.H. Kim, In-situ investigation of thermal aging effect on oxide formation in Ni-base alloy/low alloy steel dissimilar metal weld interfaces, *Corros. Sci.* 86 (2014) 295.
- [21] C. Miyake, A. Nakatani, T. Isobe, Electron spin resonance study of oxide films on Zircaloy claddings - Part (I), *J. Nucl. Mater.* 217 (1994) 172.
- [22] H.S. Hong, S.J. Kim, K.S. Lee, Effects of alloying elements on the tensile properties and oxidation behavior of modified Zircaloy-4 in 360°C water, *J. Nucl. Mater.* 238 (1996) 211.
- [23] P. Barberis, T. Merle-Méjean, P. Quintard, On Raman spectroscopy of zirconium oxide films, *J. Nucl. Mater.* 246 (1997) 232.
- [24] H.S. Hong, S. Jin Kim, K. Sub Lee, Long-term oxidation characteristics of oxygen-added modified Zircaloy-4 in 360°C water, *J. Nucl. Mater.* 273 (1999) 177.
- [25] J. Krýsa, J. Maixner, P. Matějka, V. Vrtílková, Structure and composition of zirconium oxide films formed in high pressure water with different Li⁺ concentration at 360 °C, *Mater. Chem. Phys.* 63 (2000) 1.
- [26] J.H. Kim, I.S. Hwang, Development of an in situ Raman spectroscopic system for surface oxide films on metals and alloys in high temperature water, *Nucl. Eng. Des.* 235 (2005) 1029.
- [27] Y. Qiu, T. Shoji, Z. Lu, Effect of dissolved hydrogen on the electrochemical behaviour of Alloy 600 in simulated PWR primary water at 290 °C, *Corro. Sci.* 53 (2011) 1983.
- [28] F. Meng, Z. Lu, T. Shoji, J. Wang, E.-h. Han, W. Ke, Stress corrosion cracking of uni-directionally cold worked 316NG stainless steel in simulated PWR primary water with various dissolved hydrogen concentrations, *Corro. Sci.* 53 (2011) 2558.
- [29] A. Loucif, J.P. Petit, Y. Wouters, Semiconducting behavior and bandgap energies of oxide films grown on alloy 600 under PWR simulated primary water conditions with different dissolved hydrogen contents, *J. Nucl. Mater.* 443 (2013) 222.
- [30] B. Wadman, H.O. André, Zirconium in the Nuclear Industry: Ninth International Symposium, Kobe, Japan, ASTM International. 1132 (1990) 461.
- [31] D. Hudson, G.D.W. Smith, Initial observation of grain boundary solute segregation in a zirconium alloy (ZIRLO) by three-dimensional atom probe, *Scr. Mater.* 61 (2009) 411.
- [32] N. Ni, D. Hudson, J. Wei, P. Wang, S. Lozano-Perez, G.D.W. Smith, J.M. Sykes, S.S. Yardley, K.L. Moore, S. Lyon, R. Cottis, M. Preuss, C.R.M. Grovenor, How the crystallography and nanoscale chemistry of the metal/oxide interface develops during the aqueous oxidation of zirconium cladding alloys, *Acta Mater.* 60. (2012) 7132.
- [33] B.-K. Kim, H.-o. Hamaguchi, Mode Assignments of the Raman Spectrum of Monoclinic Zirconia by Isotopic Exchange Technique, *Phys. Status Solidi (b)*. 203 (1997) 557.
- [34] Y.-s. Kim, Y.-h. Jeong, S.-b. Son, A study on the effects of dissolved hydrogen on zirconium alloys corrosion, *J. Nucl. Mater.* 444 (2014) 349.
- [35] H. Okamoto, O-Zr (Oxygen-Zirconium), *J. Phase Equilib. Diff.* 28 (2007) 498.
- [36] C. Phillippi, K. Mazdizyasni, Infrared and Raman spectra of zirconia polymorphs, *J. Am. Ceram.* 54 (1971) 254.
- [37] H.-G. Kim, J.-Y. Park, B.-K. Choi, Y.-H. Jeong, Evaluation of pre-transition oxide on Zr-0.4 Nb alloy by using the HVEM, *J. Nucl. Mater.* 374 (2008) 204.
- [38] J.S. Moya, M. Diaz, J.F. Bartolomé, E. Roman, J.L. Sacedon, J. Izquierdo. Zirconium oxide film formation on zircaloy by water corrosion, *Acta Mater.* 48. (2000) 4749.